Journal of Hazardous Materials 514 (2026) 142776

Contents lists available at ScienceDirect

Journal of Hazardous Materials

journal homepage: www.elsevier.com/locate/jhazmat

Dynamic capillary barrier failure in stratified media: A dimensionless framework for LNAPL redistribution under water table fluctuations

Didi Li [a], Kun Luo [a], Zhimin Ao [b,*]

[a] Guangdong Key Laboratory of Environmental Catalysis and Health Risk Control, Guangdong-Hong Kong-Macao Joint Laboratory for Contaminants Exposure and Health, School of Environmental Science and Engineering, Guangdong University of Technology, Guangzhou 510006, China
[b] School of Technology for Sustainability, Advanced Interdisciplinary Institute of Environment and Ecology, Beijing Normal University, Zhuhai 519087, China

HIGHLIGHTS

- Framework (η_{max}, Bo^*, Ca^*) predicts LNAPL redistribution and aquifer vulnerability.
- Dual thresholds ($\eta_{max} \geq 1.0$, $Bo^* > 1.0$) dictate F-C capillary barrier failure.
- Lower Ca^* significantly promotes lateral toxic plume expansion at C-F interfaces.
- Model prevents the underestimation of hazardous footprints in dynamic aquifers.

GRAPHICAL ABSTRACT

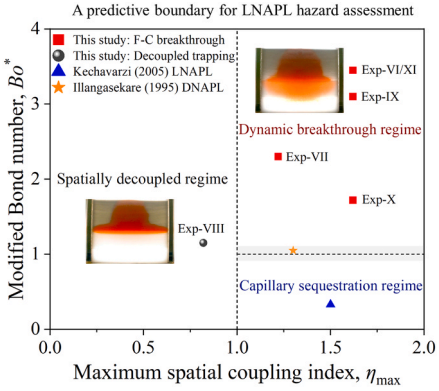

ARTICLE INFO

Keywords:
LNAPL redistribution
Water table fluctuation
Stratified porous media
Capillary barrier failure
Dimensionless analysis

ABSTRACT

Subsurface contamination by light non-aqueous phase liquids (LNAPLs) poses long-term environmental risks, which is significantly influenced by the dynamic coupling of transient water table fluctuations (WTFs) and stratigraphic heterogeneity. To assess aquifer vulnerability and decouple these multiscale physical processes, we propose a macroscopic dimensionless framework governing dynamic LNAPL redistribution and capillary barrier failure. Within this framework, three key dimensionless parameters are established: a maximum spatial coupling index (η_{max}) defines the spatial continuity prerequisite for transient pressure transmission; a modified Bond number (Bo^*) determines the macroscopic threshold for hydraulically driven interfacial capillary barrier failure; and a macroscopic capillary number (Ca_{macro}) scales the kinetic competition between vertical contaminant penetration and lateral spreading. By factoring out the constant geometric constraints of our specific quasi-2D experimental setup, the dynamic component of this kinetic regulator is further isolated as a system-level parameter (Ca^*). To validate this theoretical approach, systematic 2D sandbox experiments were conducted within stratified systems featuring distinct coarse-over-fine (C-F) and fine-over-coarse (F-C) interfaces under varying WTF amplitudes, initial water tables, and fluctuation rates. The experimental results reveal that LNAPL redistribution in F-C structures follows a threshold-controlled mechanism governed by macroscopic displacement

* Corresponding author.
E-mail address: zhimin.ao@bnu.edu.cn (Z. Ao).

https://doi.org/10.1016/j.jhazmat.2026.142776
Received 31 March 2026; Received in revised form 31 May 2026; Accepted 19 June 2026
Available online 20 June 2026

pressure, closely matching the dual critical breakthrough conditions of $\eta_{max} \geq 1.0$ and $Bo^* > 1.0$. Conversely, C-F structures lacking interfacial capillary barriers exhibit a rate-dependent allocation mechanism, where lower Ca^* values significantly promote lateral hazardous plume expansion via pore-scale capillary wicking compared to high-rate conditions. External validation across multiple fluid datasets confirms that this framework provides a first-order predictive boundary, offering essential guidelines for evaluating contaminant fate, capillary barrier stability, and overall environmental risk in highly dynamic groundwater systems.

1. Introduction

Subsurface contamination by light non-aqueous phase liquids (LNAPLs), such as petroleum hydrocarbons, remains a global environmental challenge due to their long-term persistence and significant ecotoxicity [1,2]. Once released, LNAPL migration is governed by the dynamic interaction between macroscopic gravitational driving forces and pore-scale capillary resistance. When the infiltration flux overcomes the capillary entry pressures of the porous media, LNAPL can migrate further downward to the top of the saturated zone and undergo lateral spreading, directly threatening groundwater quality [3,4]. In heterogeneous subsurface environments, stratified architectures (e.g., fine-coarse sand interbeds) strictly regulate these migration pathways. Interface effects in these formations, such as macroscopic capillary barriers at fine-over-coarse (F-C) interfaces and flow retardation in coarse-over-fine (C-F) sequences, significantly alter the spatiotemporal distribution patterns of LNAPL plumes [5,6]. Recent studies have highlighted that stratigraphic sequences and interface inclination can induce preferential flow diversion, fundamentally changing the migration footprint [7,8].

In shallow aquifers, water table fluctuations (WTFs) driven by seasonal variations or anthropogenic activities serve as a primary transient hydrodynamic forcing that dynamically reshapes the contaminant plume. WTFs can significantly alter pore water pressure, driving multiphase fluid displacement and reshaping the capillary fringe [9]. Previous research has demonstrated that WTFs induce dynamic redistribution among free, dissolved, and residual phases through pore-scale trapping and mobilization during drainage and imbibition cycles [1,10,11]. Despite the recognized importance of transient hydrodynamics [12–15], the fundamental coupling mechanisms between WTF perturbations and subsurface heterogeneities remain inadequately quantified.

In these stratified configurations, the transient local water content dictated by WTFs acts as the key variable controlling cross-interface migration [16]. By dynamically altering pore-water displacement and the macroscopic pressure balance, WTFs compromise the retention function of capillary barriers, rather than altering the intrinsic physical properties of the geological media itself, thereby triggering secondary LNAPL mobilization. Although recent studies have observed that WTFs facilitate horizontal expansion [17] and that dual-lithology systems strengthen LNAPL retention [18], the current literature predominantly relies on empirical parametric variations (e.g., independently varying WTF amplitudes or fluctuation rates) to describe the changing migration footprint [19]. Such empirical approaches lack a fundamental mechanical scaling basis. Because local multiphase flow behavior is strictly regulated by fluid-specific properties and pore-scale capillary resistance, the macroscopic phenomena observed in specific laboratory geometries cannot be reliably upscaled or extrapolated to complex field scenarios. This limitation arises because macroscopic empirical observations conflate two distinct physical mechanisms: threshold-driven interfacial breakthrough, which requires sufficient transient pressure, and rate-dependent lateral spreading, which is governed by kinetic relaxation times. Without decoupling these competing multi-scale forces, the true environmental risk and the potential for toxic plume expansion in dynamic aquifers remain unpredictable. To conceptualize this inherently transient and heterogeneous nature of LNAPL redistribution, there is an urgent need to transition from qualitative descriptions to a generalized and physics-based dimensionless scaling framework.

To clarify the complex multiphase interactions under dynamic conditions, we present a conceptual schematic (Fig. 1) detailing the transient redistribution of an LNAPL spill within a stratified unconfined aquifer. Upon release, the LNAPL migrates downward, leaving a trail of residual ganglia before accumulating as a free-phase pool above the stratigraphic interface (the capillary barrier). Meanwhile, a dissolved plume develops within the saturated zone and the capillary fringe. The dynamic interaction between this trapped LNAPL pool and the fluctuating groundwater is governed by three theoretical prerequisites. First, the maximum spatial coupling index (η_{max}) dictates whether the peak elevation of the dynamic capillary fringe physically contacts the LNAPL interface. Upon successful spatial coupling ($\eta_{max} \geq 1.0$), the subsequent allocation of the LNAPL fluxes is determined by a dual-mechanism process: the modified Bond number (Bo^*) represents the critical pressure threshold for hydraulically driven interfacial instability (i.e., vertical breakthrough) into the lower stratum, while the macroscopic capillary number (Ca_{macro}) regulates the kinetically-limited lateral spreading along the interface. This conceptual framework serves as the theoretical blueprint for our subsequent scaling analysis. Through this analysis, we established a fully quantified phase diagram (presented in Section 4.4) that validates these boundaries using both our experimental results and external literature datasets.

The primary objective of this study is to establish a generalized dimensionless framework that governs LNAPL redistribution under dynamic WTFs, thus providing a physical basis for evaluating aquifer vulnerability to hazardous spills. We first propose a theoretical regime map based on fundamental multiphase principles, defining the exact dimensionless parameters, i.e., a maximum spatial coupling index (η_{max}), a modified Bond number (Bo^*), and a macroscopic capillary number (Ca_{macro}). For application to our specific quasi-2D experimental setup, the dynamic component of this kinetic regulator is further isolated as a system-level modified capillary number (Ca^*). Together, these parameters dictate interfacial capillary barrier failure and kinetic lateral allocation. Subsequently, to validate this theoretical framework, systematic 2D sandbox experiments were conducted within stratified systems featuring distinct C-F and F-C interfaces subjected to varying WTF amplitudes, initial water levels, and fluctuation rates. By integrating our highly transient experimental observations with classical macroscopic benchmark datasets, this study supports the robustness of the proposed framework, thereby providing a physically reliable predictive boundary for dynamic subsurface risk assessment and targeted remediation design.

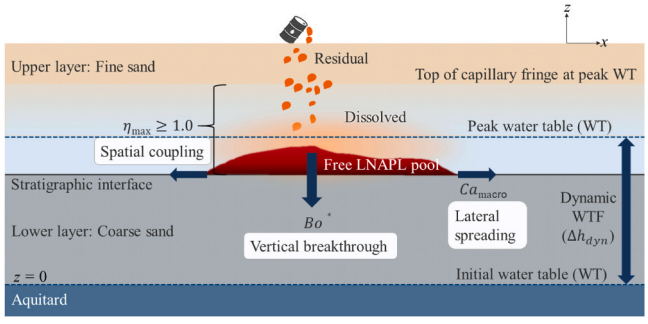

Fig. 1. Transient subsurface LNAPL redistribution under dynamic water table conditions in the upper fine and lower coarse sand layers.

2. Materials and methods

2.1. Materials

To ensure optical clarity for real-time visualization, fused quartz sand (Linzhi Quartz Company, China) with a high SiO_2 purity ($\geq$ 99.5%) was utilized. This material provides the necessary transparency for quantitative image analysis of multiphase flow [20]. Two grain sizes were selected: coarse sand (C, 20–40 mesh) and fine sand (F, 40–70 mesh) to simulate stratigraphic heterogeneity. The grain size distribution of the quartz sands was characterized using the sieving method. Porosity was determined using the water immersion method, while permeability and bulk density were measured based on Darcy's law and the volumetric method, respectively. The main physical properties are presented in Table 1. Both materials exhibit low uniformity coefficient ($C_u = d_{60}/d_{10}$) values (< 1.5), indicating a highly uniform pore structure that helps controlled multiphase flow experiments.

Deionized (DI) water with a density of 984 kg/m^3 served as the wetting phase. The LNAPL phase consisted of 0# diesel (China Petrochemical Corporation), stained with 0.05 g/L Sudan III dye to facilitate optical tracking. Sudan III was chosen for its excellent integration with the oil phase, ensuring stable visualization without altering fluid properties [21,22]. The density (ρ) and dynamic viscosity (μ) of the diesel are 839 kg/m^3 and 3.2 mPa·s at 25 °C, respectively (data provided by the supplier). The interfacial tension (σ_{ow}) between the diesel and DI water at 25 °C was measured as 34.855 ± 0.030 mN/m using the Wilhelmy plate method with a DCAT21 tensiometer (DataPhysics Instruments, Germany).

The soil-water characteristic curves (SWCCs) and soil-oil characteristic curves (SOCCs) for the two types of quartz sand are shown in Fig. 2. Similar to an SWCC, an SOCC defines the fundamental relationship between the volumetric oil content and the macroscopic capillary pressure head, thereby characterizing the specific retention capacity of the porous medium for the oil phase. These curves were determined using the sand core funnel method [23,24], which simultaneously measures the volumetric liquid (water or diesel) content and the capillary head to characterize the retention capacity of each sand type. Here, the volumetric liquid content (θ, cm^3/cm^3) is defined as the ratio of the liquid volume to the total volume of the porous medium. It should be noted that while θ is proportional to fluid saturation (S, the ratio of liquid volume to the pore volume, $S = \theta$/porosity), the volumetric liquid content is consistently utilized as the standard physical quantity for both presenting the retention curves and fitting the van Genuchten (VG) model. To ensure consistency in the capillary head unit across different fluid systems, the measured diesel column heights were converted into equivalent water heads using the density ratio of diesel to water (i.e., 839/984).

The SOCCs for the fine sand consistently plotted above those for the coarse sand, indicating significantly higher capillary heads at equivalent liquid contents. Notably, the difference between coarse and fine sand was more pronounced in the SOCCs than in the SWCCs. This suggests that the capillary retention behavior is inherently more dominant for the oil phase, likely due to the enhanced sensitivity of the capillary pressure to variations in pore-throat geometry compared to the water phase.

The experimental data were fitted using the VG model [25]:

$$\theta(h) = \theta_r + \frac{\theta_s - \theta_r}{[1 + (\alpha h)^n]^m} \quad (1)$$

where θ is the volumetric liquid content at a specific capillary head h, θ_r is the residual liquid content, θ_s is the saturated liquid content, α is a scaling parameter inversely related to the displacement pressure, n is the pore-size distribution index, and m is the shape parameter, typically constrained by $m = 1 - 1/n$.

The displacement pressure (h_d) for different porous media and fluid combinations was determined using the maximum tangent method. Specifically, based on the fitted parameters of the VG model, the true inflection point of the retention curve was analytically identified by locating the root of the second derivative ($\frac{d^2\theta}{dh^2} = 0$). A tangent line representing the maximum specific liquid capacity was then drawn at this inflection point. The macroscopic displacement pressure, h_d, was defined as the capillary head corresponding to the intersection of this tangent line and the horizontal line representing the saturated fluid content ($\theta = \theta_s$). The complete fitting parameters and the calculated h_d values are summarized in Table 2. To quantify the parameter estimation uncertainty, the standard errors and 95% confidence intervals for all VG model parameters are detailed in Table S1 of the Supporting Information (SI).

Theoretically, according to the Leverett J-function scaling and the Young-Laplace equation, the displacement pressure h_d is expected to be proportional to the interfacial tension. Given that the air-diesel interfacial tension is significantly lower than that of the air-water system, the measured $h_{d(oil)}$ should be lower than $h_{d(water)}$ for the same porous media. However, our results exhibit a notable deviation from this classical scaling in both media: the $h_{d(oil)}$ failed to scale proportionally in the coarse sand, and unexpectedly deviated in the fine sand, where $h_{d(oil)}$ (22.2 cm) exceeded $h_{d(water)}$ (18.6 cm). This suggests that factors beyond bulk interfacial tension dominate the capillary behavior in finer pore-throat geometries. One plausible explanation is the significant reduction in the effective pore-throat radius. As a complex mixture of hydrocarbons, diesel may contain heavier or polar compounds that can adsorb onto the large specific surface area of the fine quartz sand, creating microscopic boundary layers and inducing localized wettability alteration (shifting towards intermediate-wet conditions, which dynamically alters the effective contact angle). This can hinder the pore throats. Furthermore, the significantly higher residual content (θ_r = 0.214) observed in the fine sand SOCC suggests that LNAPL may trigger pore-scale redistribution or particle re-arrangement, effectively constricting the primary flow pathways and leading to an unexpectedly high macroscopic displacement pressure. These findings underscore the limitations of using simple interfacial tension scaling to predict LNAPL retention in complex fine-grained subsurface environments.

2.2. Experimental setup

As illustrated in Fig. 3, a two-dimensional sand tank system was constructed to enable real-time monitoring of LNAPL redistribution. The sand tank was constructed from 8-mm-thick acrylic panels, with internal dimensions of 70 cm (length) × 60 cm (height) × 2 cm (width). It featured a central 60-cm-long porous media zone, flanked by two 5-cm-wide water table control zones. The porous media zone was filled with coarse and fine sands, each forming a 25-cm-thick layer, to simulate two typical stratified configurations: coarse-over-fine (C-F) and fine-over-coarse (F-C). During packing, the tank walls were gently tapped with a rubber hammer after every 5 cm of quartz sand was laid to ensure uniform and compact density.

A permeable partition, composed of a double-layer acrylic screen

Table 1
Physical properties of the fused quartz sands used in the experiments.

Sand	d_{10} (mm)	d_{50} (mm)	d_{60} (mm)	C_u (-)	Porosity (-)	Permeability (m^2)	Bulk density (kg/m^3)
Coarse	0.46	0.58	0.61	1.33	0.44	1.09×10^{-11}	1260
Fine	0.22	0.24	0.26	1.18	0.36	4.07×10^{-12}	1220

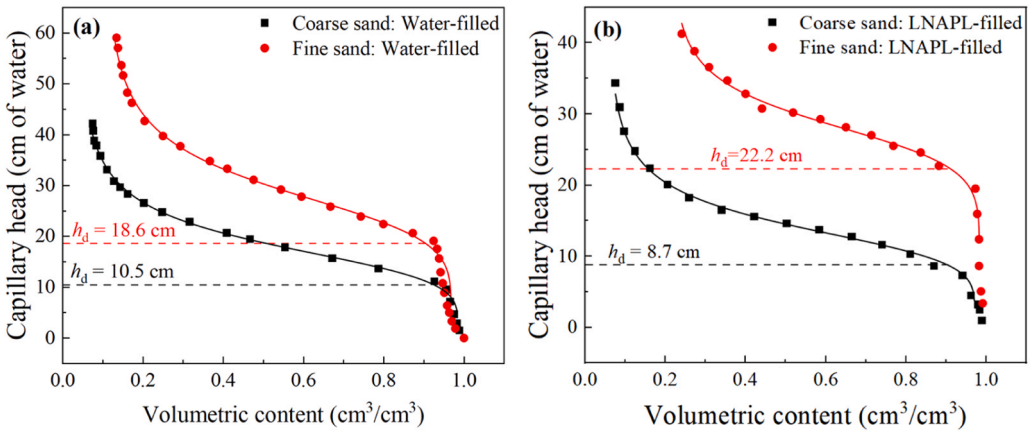

Fig. 2. Capillary head characteristics of sand media. (a) Soil-water characteristic curves (SWCCs), and (b) soil-oil characteristic curves (SOCCs). Solid lines represent van Genuchten (VG) model fits to experimental data (scattered points).

Table 2
Analytic results of VG model and displacement pressures.

Sand	Fluid	θ_s (-)	θ_r (-)	α (cm^{-1})	n (-)	h_d (cm)
Coarse	Water	0.985	0.038	0.0577	4.883	10.5
Coarse	LNAPL	0.971	0.055	0.0737	5.309	8.7
Fine	Water	0.968	0.103	0.0357	5.701	18.6
Fine	LNAPL	0.985	0.214	0.0355	9.033	22.2

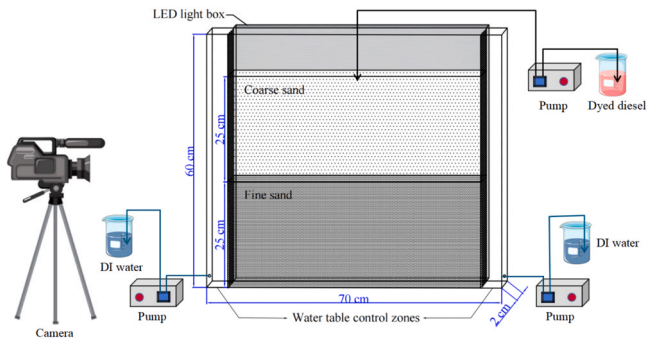

Fig. 3. Schematic representation of the sand tank experimental system.

with a 200-mesh stainless steel screen sandwiched in between, was installed between the porous media zone and the water table control zones. This design maintained hydraulic connection while preventing particle migration into the control zones during WTFs. LNAPL was introduced at the tank center through a peristaltic pump and a fine needle. WTFs were regulated through the 3-mm-diameter adjustment hole located 2 cm above the tank base in each water table control zone. To ensure uniform illumination, a 28 W LED light box (60 cm × 60 cm) served as the backlight source, with a diffuser panel placed between the light box and the sand tank. Images were captured at a resolution of 2880 × 2160 using a tripod-mounted camera. Subsequent quantitative extraction of LNAPL contamination areas and migration distances was performed via manual tracing using ImageJ software. Detailed uncertainty quantification regarding this image processing method is provided in **Text S1** of the SI.

As shown in Table 3, eleven sets of experiments were conducted to isolate the effects of stratified structures (C-F and F-C), WTF amplitudes, fluctuation rates, initial WT heights. Experiments I (C-F) and VI (F-C) served as the baselines, characterized by no initial WT, a 30-cm WTF amplitude, and a 40 mL/min fluctuation rate. Against these baselines, four comparative scenarios were designed for each structure to evaluate amplitude (20 cm, 10 cm), initial water Table (3 cm), and fluctuation

Table 3
Experimental scenarios and water table fluctuation (WTF) parameters.

Experiment	Layer structure	Initial WT (cm)	Fluctuation amplitude (cm)	Fluctuation rate (mL/min)	WTF cycles
I	C-F	0	0–30–0	40	2
II	C-F	0	0–20–0	40	2
III	C-F	0	0–10–0	40	2
IV	C-F	3	3–30–3	40	2
V	C-F	0	0–30–0	20	2
VI	F-C	0	0–30–0	40	2
VII	F-C	0	0–20–0	40	2
VIII	F-C	0	0–10–0	40	2
IX	F-C	3	3–30–3	40	2
X	F-C	15	15–30–15	40	2
XI	F-C	0	0–30–0	20	2

rate (20 mL/min). Notably, an additional high initial water table scenario (15 cm, Exp-X) was specifically conducted for the F-C structure to investigate the effects of complete interfacial submergence.

All experiments uniformly involved the injection of 120 mL of diesel into the sand layer at a rate of 5 mL/min over 24 min, followed by a 12-h settling period to allow natural migration of the diesel. After settling, DI water was pumped into the water table control zone at specified rates (Table 3) to gradually raise the water table to the target height. The water table maintained stable for 40 min before being lowered at the same rate, returning it to the initial water table, followed by another 24-h settling period to complete the first WTF cycle. A second identical fluctuation cycle was then conducted to examine the effect of multiple fluctuations on diesel migration and redistribution.

3. A dimensionless framework for interfacial capillary barrier stability under dynamic groundwater fluctuations

The redistribution of LNAPL in stratified porous media under WTFs is governed by a dynamic competition among transient hydraulic gradients, pore-scale capillary resistance, and the characteristic relaxation time of the multiphase system. Conventional static capillary equilibrium assumptions typically fail to capture the interfacial instability triggered by such transient pressure perturbations. To conceptualize and predict these diverse redistribution trajectories beyond the specific experimental geometry, we propose a generalized dimensionless framework.

This framework explicitly decouples these multiscale physical processes into three sequential controlling regimes: (1) a spatial precondition, governed by a maximum coupling index (η_{max}), which dictates whether transient hydraulic perturbation can physically reach the heterogeneous interface; (2) a macroscopic pressure-driven threshold

for interfacial instability (i.e., vertical breakthrough), defined by a modified Bond number (Bo^*); and (3) a rate-dependent distribution regime, regulated by a modified capillary number (Ca^*), which controls the dynamic competition between vertical penetration and lateral spreading.

3.1. Spatial coupling and physical switch for pressure transmission (η_{max})

The fundamental prerequisite for WTF-induced LNAPL redistribution is the continuous transmission of transient pore-water pressure to the trapped contaminant plume. To quantify this spatial continuity requirement, we define the maximum spatial coupling index ($\eta_{\max}$) as the ratio of the peak capillary fringe height to the interface depth:

$$\eta_{\max} = \frac{h_{\max} + h_{\text{rise}}}{Z_{\text{int}}} \tag{2}$$

where $h_{\max}$ is the peak water table during fluctuation, h_{rise} is the characteristic capillary rise of the geologic stratum hosting the fluctuating water table (quantitatively represented in this framework by its macroscopic water-phase displacement pressure head, $h_{\text{d(water)}}$), and Z_{int} is the elevation of the stratified interface relative to the same reference datum.

This index serves as a binary physical switch that transitions at the critical value of 1.0. When $\eta_{\max} < 1.0$, the peak elevation of the capillary water is lower than the interface elevation. Consequently, the capillary fringe fails to bridge the gap to the interface and the system remains in a spatially decoupled state. In this regime, the dynamic hydraulic head (Δh_{dyn}) is dissipated within the continuous air phase, rendering the WTF perturbation incapable of exerting work on the trapped LNAPL. Conversely, when $\eta_{\max} \geq 1.0$, the water phase achieves continuity across the interface, enabling the transmission of transient hydraulic gradients and transitioning the system into a dynamic response regime.

3.2. Interfacial pressure balance and the threshold for dynamic breakthrough (Bo^*)

Once the spatial coupling condition is satisfied ($\eta_{\max} \geq 1.0$), the functional failure of the interfacial capillary barrier in the F-C structure is governed by the macroscopic balance between the transient hydraulic driving force and the intrinsic pore-scale capillary resistance. The macroscopic driving force originates from the transient head difference induced by water table rise or fall, expressed as $P_{driving} = \rho_w g \Delta h_{dyn}$. The core resistance of the interface stems from the displacement pressure of the pore throats at the heterogeneous interface. For the F-C structure undergoing downward breakthrough, this is primarily controlled by the entry value of the underlying coarse sand, i.e., $P_{resisting} = \rho_w g h_{d(oil),coarse}$. It should be noted that the interfacial instability triggering this breakthrough is not a density-driven Rayleigh-Taylor instability, as the lighter LNAPL residing above the denser water phase forms a gravitationally stable configuration. Instead, it refers to a hydraulically driven functional failure of the capillary barrier, i.e., macroscopic invasion percolation. Because downward breakthrough physically requires the non-wetting phase to displace the pore water of the underlying stratum, this interfacial resisting force is dictated by the capillary entry pressure of the invaded coarse medium, independent of the overlying fine sand's retention capacity.

As highlighted in fundamental multiphase flow scaling analyses [26, 27], macroscopic scaling often incorporates a structural aspect ratio (L/d) to connect the macroscopic driving length scale to the characteristic pore-scale dimension. While this aspect ratio is required for the macroscopic capillary number (Ca_{macro}) to capture spatial flow field constraints, the vertical breakthrough governed by hydraulic head is inherently a pressure-threshold phenomenon, rather than a kinetically limited viscous flow process. Furthermore, deriving a representative pore-throat diameter (d) directly from idealized geometric approximations or statistical distributions introduces significant uncertainty, as it fails to capture the effective radius of the critical interconnected pore-throats that regulate macroscopic invasion percolation.

To scale these competing forces without relying on idealized geometric approximations, we define the modified Bond number (Bo^*) as a macroscopic pressure ratio. According to the Young-Laplace physics, the macroscopic displacement pressure head (h_d) is the effective continuum-scale representation of the capillary entry pressure for those critical interconnected pore-throats. Therefore, the modified Bond number (Bo^*) which represents the macroscopic pressure-driven threshold for interfacial instability, is formulated as:

$$Bo^* = \frac{\Delta h_{dyn}}{h_{d(oil),coarse}} \tag{3}$$

where Δh_{dyn} is the actual dynamic head generated during the drawdown phase (i.e., $h_{\max} - h_{\text{initial}}$). By normalizing both Δh_{dyn} and $h_{d(oil),coarse}$ to equivalent water heads (Section 2.1), the dimensionless integrity of Bo^* is fully preserved. The gravitational component of the LNAPL phase is considered negligible relative to the significantly larger induced hydraulic gradient under these active dynamic conditions. To ensure the physical rigor of this dimensionless analysis, the resisting term should be characterized by media-specific soil-oil characteristic curves (SOCCs), aiming to capture the exact multi-phase capillary resistance rather than relying on idealized interfacial tension scaling.

By synthesizing the above two governing parameters, the theoretical phase space is partitioned into three distinct stability regimes (Fig. 4). When $\eta_{\max} < 1.0$, the system falls into the spatially decoupled regime, where the dynamic perturbation is physically blocked regardless of the hydraulic head. When $\eta_{\max} \geq 1.0$ but $Bo^* < 1.0$, the system enters the capillary sequestration regime, indicating that the transient pressure successfully reaches the interface but is hydrostatically insufficient to overcome the pore-throat resistance. Only when both conditions are satisfied ($\eta_{\max} \geq 1.0$ and $Bo^* \geq 1.0$) does the system transition into the dynamic breakthrough regime, where the pressure threshold is breached and this hydraulically driven interfacial instability is actively triggered. Fig. 4 illustrates these purely theoretical regime boundaries based on our mathematical derivations, while the fully quantified phase diagram plotting specific empirical values from our physical models and literature datasets is presented in **Section 4.4.1**, Fig. 12.

3.3. Kinetic competition and the system-level modified capillary number (Ca^*)

Unlike the pressure-threshold governed by Bo^*, which acts as the hydraulic switch for vertical barrier failure in F-C media, the redistribution behavior in the C-F structure is fundamentally distinct. In

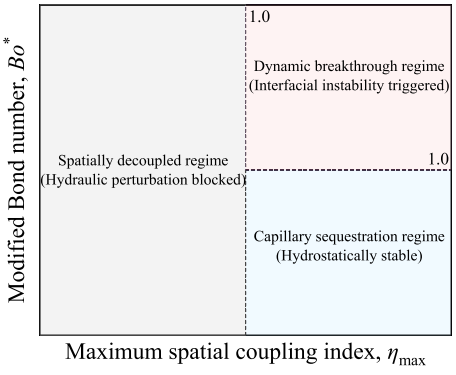

Fig. 4. Conceptual regime map defining the theoretical prerequisites and pressure thresholds for interfacial capillary barrier stability. The spatial coupling index ($\eta_{\max}$) acts as the spatial continuity switch, while the modified Bond number (Bo^*) governs dynamic breakthrough.

scenarios involving C-F configurations where the initial LNAPL gravitational potential readily exceeds the displacement pressure of the underlying fine sand, vertical penetration occurs naturally under gravity. Consequently, the primary WTF-induced environmental risk shifts from triggering vertical breakthrough (which is no longer the limiting threshold) to driving lateral spreading along the interface.

The nature of this competition is temporal. The allocation of fluid fluxes is regulated by kinetic competition between vertical macroscopic viscous displacement and pore-scale lateral capillary wicking. A faster water table fluctuation (higher effective velocity) reduces the characteristic residence time available for capillary-driven lateral spreading before the next vertical perturbation. In contrast, a slower fluctuation provides an extended temporal window for the lateral capillary wicking to develop. As demonstrated by fundamental scaling analyses [26,27], a rigorous macroscopic dimensionless capillary number incorporates both the kinetic ratio of viscous to capillary forces and a structural aspect ratio connecting the macroscopic length scale to the pore-throat dimension, i.e., $Ca_{macro} = \frac{\mu v}{\sigma} \times \frac{L}{d}$. For a given stratum within our layered system, the structural aspect ratio (L/d) remains geometrically constant. Therefore, the temporal evolution of the LNAPL redistribution is governed by the transient intensity of the system-scale forcing. To characterize this rate-dependent competition and isolate the pure transient dynamic forcing, we factor out the constant geometric term (L/d) and substitute the macroscopic Darcy velocity (v) with the effective pore velocity (v_{pore}) to accurately capture the true kinetic competition at the pore-scale fluid interfaces. Thus, we define a system-level modified capillary number (Ca^*) derived from Ca_{macro}:

$$Ca^* = \frac{\mu v_{pore}}{\sigma_{ow}} \tag{4}$$

where v_{pore} is the effective vertical velocity of the dynamic water table, equivalent to the macroscopic Darcy velocity divided by bulk porosity. Note that the true local interstitial velocity at the fluid–fluid interface is modulated by the transient wetting-phase saturation, i.e., $v_{local} \propto v_{pore}/S_w$. However, we employed the system-scale v_{pore} to construct Ca^* as a macroscopic forcing parameter. This is because the local saturation correction is embedded in the observed multiphase redistribution dynamics under the given structural constraints. Ca^* physically scales this kinetic competition. A lower fluctuation rate proportionally reduces Ca^*, thereby providing the multiphase system with an extended characteristic relaxation time. This prolonged contact duration allows the horizontal capillary wicking forces within the high-permeability coarse sand to dominate over the vertical viscous resistance.

3.4. Comparison with traditional definitions

The proposed dimensionless framework differs from conventional multiphase flow characterizations. Table 4 summarizes the theoretical distinctions between traditional formulations and the modified parameters tailored for this study. In traditional multiphase flow studies, dimensionless numbers like the standard Bond number and capillary number are widely utilized to describe pore-scale droplet mobilization and micro-model viscous sweeping efficiency [e.g., 21, 26–28]. However, these classic definitions rely heavily on pore-scale static buoyancy ($\Delta\rho g d^2$) or localized viscous forces (μv), lacking the structural scaling necessary to represent continuum-scale behavior across heterogeneous interfaces.

Table 4
Comparison of traditional and modified dimensionless numbers in multiphase flow.

Parameter	Traditional micro-scale [26–28]	Macroscopic structural scaling [26,27]	System-level modification (This study)
Bond number	$\Delta\rho g d^2/\sigma$ (Pore-scale static buoyancy)	$Bo_{macro} = \frac{\Delta\rho g L^2}{\sigma} \times \frac{d}{L}$	$Bo^* = \frac{\Delta h_{dyn}}{h_{d(oil),coarse}}$ (Dynamic pressure threshold)
Capillary number	$\mu v/\sigma$ (Pore-scale viscous sweeping)	$Ca_{macro} = \frac{\mu v}{\sigma} \times \frac{L}{d}$	$Ca^* = \frac{\mu v_{pore}}{\sigma_{ow}}$ (Dynamic fluid distribution)

As mathematically justified in our framework, the modified variables translate classic micro-scale forces into macroscopic continuum metrics. Specifically, our modified Bond number (Bo^*) replaces the traditional pore-scale static buoyancy term with a macroscopic driving head (Δh_{dyn}), establishing a direct pressure threshold for continuum-scale barrier failure. While standard macroscopic scaling includes the aspect ratio (L/d) [26,27], our study further isolates the dynamic transient forcing to define a system-level capillary number (Ca^*). This parameter specifically addresses the highly transient kinetic allocation across unconstrained macroscopic interfaces.

4. Experimental validation of the framework

To empirically validate the proposed dimensionless framework, systematic 2D sandbox experiments were conducted. By independently varying WTF amplitudes, initial water tables, and fluctuation rates across distinct C-F and F-C interfaces, we aimed to transition the system across the predicted theoretical regimes and verify the deterministic roles of $\eta_{\max}$, Bo^*, and Ca^*.

4.1. Validating pressure thresholds (Bo^*) via WTF amplitudes

According to the proposed framework, WTF amplitude serves as the primary driver for Δh_{dyn}, governing the macroscopic pressure balance (Bo^*). Fig. 5 compares the LNAPL distribution in C-F and F-C layered structures during two WTF cycles with three different fluctuation amplitudes (0–30 cm−0, 0–20 cm−0, and 0–10 cm−0). The corresponding contamination area and the lateral migration distance along the stratigraphic interface are shown in Fig. 6. Prior to the onset of WTFs, the LNAPL distribution patterns in identical stratigraphic configurations were generally consistent (first column in Fig. 5). Moreover, both the contamination area and the lateral migration distance at the interface were highly similar for these identical configurations (Fig. 6). To assess experimental uncertainty, all baseline and comparative scenarios were conducted in duplicate. The standard deviations of the contamination areas across these repeated trials are provided in Figure S1 of the SI, demonstrating the high macroscopic reproducibility of the system. These results demonstrate the high reproducibility of the experiments. The minor variations observed in distribution morphology and contamination area are likely attributed to the slight heterogeneity in the sand packing.

4.1.1. Contrasting migration patterns during the natural migration stage

The migration behavior differed fundamentally between the two stratigraphic configurations. In the C-F configuration, once LNAPL reached the interface, it readily penetrated into the underlying fine sand and continued its downward migration under gravity, ultimately reaching the tank base. This is because the gravitational potential of the LNAPL plume exceeded the displacement pressure of the underlying fine sand. The overall LNAPL distribution exhibited a profile that was narrower in the upper coarse layer and wider in the lower fine layer by the end of the natural migration stage (Fig. 5a_1, 5b_1 and 5c_1). In contrast, in the F-C configuration, the downward migration of LNAPL was significantly inhibited at the interface by the macroscopic capillary barrier effect. The significant difference between the soil-oil characteristic curves (SOCCs) of the fine and coarse sands (Fig. 2b) indicates high interfacial capillary resistance at the F-C interface. Consequently, LNAPL infiltration was effectively inhibited, forcing the downward momentum to dissipate into lateral spreading along the interface. By the end of the natural migration stage, most of the contaminant was retained within the overlying fine sand, with only limited amounts entering the

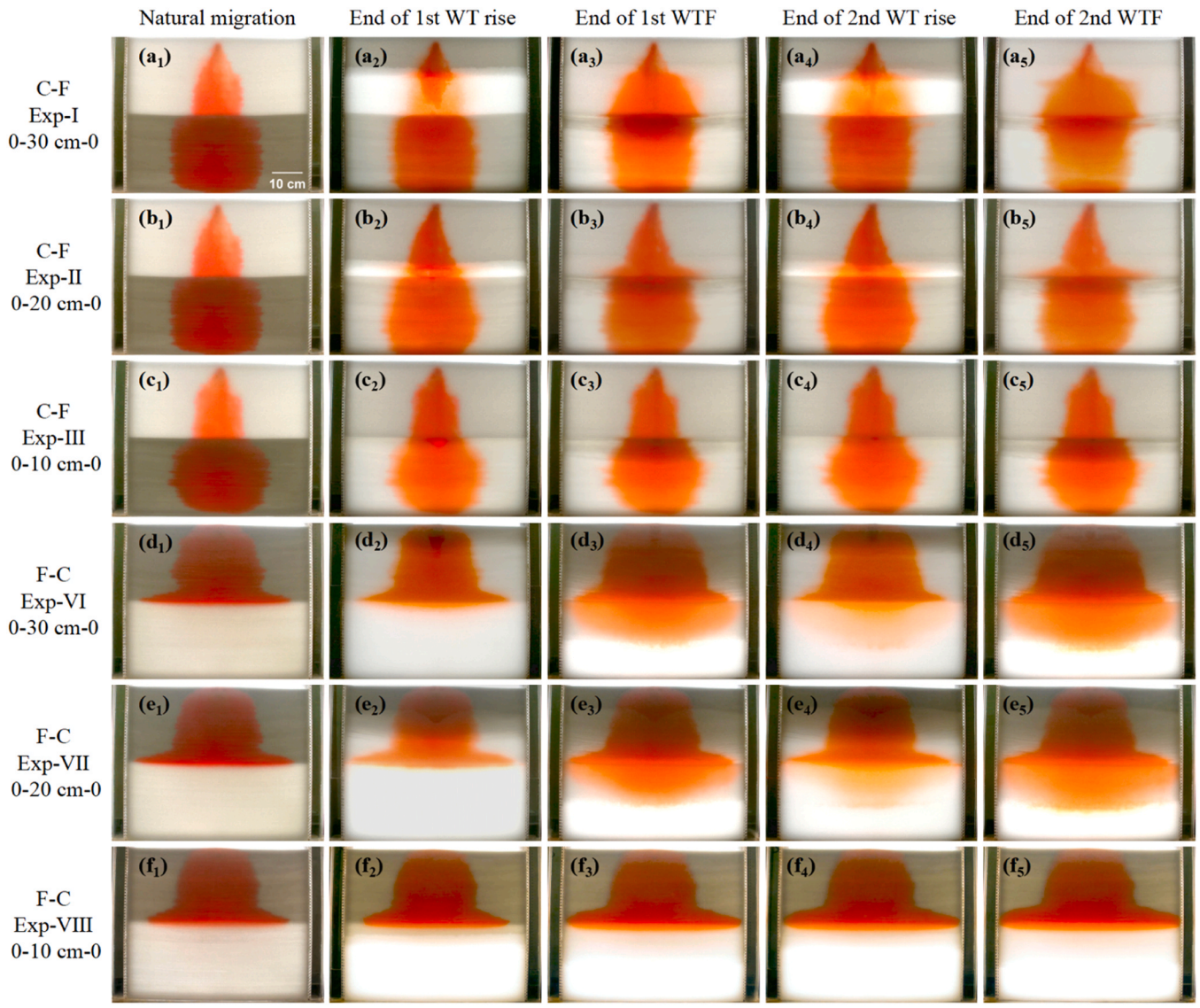

Fig. 5. Spatiotemporal distributions of LNAPL in C-F and F-C configurations, emphasizing the effects of different fluctuation amplitudes (30 cm, 20 cm, and 10 cm). The initial water table for all scenarios in this figure was set to a dry baseline of 0 cm, meaning the saturated zone begins at the bottom of the tank prior to the fluctuations. Scale bar = 10 cm in the first sub-panels.

underlying coarse sand (Fig. 5d_1, 5e_1 and 5f_1).

4.1.2. Phase-specific responses to WTFs: Accumulation and breakthrough

The introduction of WTFs acted as a transient hydraulic perturbation that reshaped the LNAPL plume according to the induced pressure gradients. The redistribution of LNAPL exhibited distinct physical mechanisms during the rising and falling phases of the water table. During the initial water table rise phase, the primary mechanism was upward hydraulic displacement. In the C-F structure, the impact of WTFs was concentrated in the upper coarse sand layer. As the capillary fringe rose across the interface, there was visual accumulation of LNAPL at the upper boundary of the capillary fringe (Fig. 5a_2, 5b_2 and 5c_2). This phase served as a preparatory stage where LNAPL was mobilized vertically, though its overall morphology remained constrained by the rising water front. In the F-C structure, the rising water table effectively compressed the LNAPL plume against the fine-grained side of the interface. For amplitudes of 20 and 30 cm, only localized diffusion occurred at the edges of the plume, as the interfacial capillary barrier remained intact despite the increased pore water pressure. In contrast, the capillary fringe only reached a height of 20.5 cm (10 + 10.5 cm) for amplitude of 10 cm (Exp-VIII, Fig. 5f_2). This resulted in a critical spatial gap of 4.5 cm below the stratified interface (located at 25 cm). This condition yields an $\eta_{max} \approx 0.82 < 1.0$, leaving the trapped LNAPL body largely undisturbed during this phase. This complete entrapment suggests a strict spatial decoupling between the WTF perturbation and the interface (corresponding to the spatially decoupled regime in Fig. 4).

The most significant redistribution occurred during the water table decline, where the combined effects of gravity and transient hydraulic gradients triggered barrier instability. In the C-F structure, the falling phase allowed LNAPL to redistribute within the now-desaturated coarse pores above the interface. The lateral migration distance reached its maximum at the layered interface, where the residual water content in the underlying fine sand provided sufficient pore-scale capillary resistance to deflect vertical flow into horizontal spreading. In the F-C configuration, the 30 cm and 20 cm amplitudes satisfied the spatial coupling prerequisite ($\eta_{max} \geq 1.0$) and generated Bo_* values well above 1.0 (specifically, 3.45 and 2.30), actively triggering interfacial instability (falling into the dynamic breakthrough regime, Fig. 4). They provided sufficient driving pressure to overcome the non-wetting displacement pressure of the underlying coarse sand, and facilitated

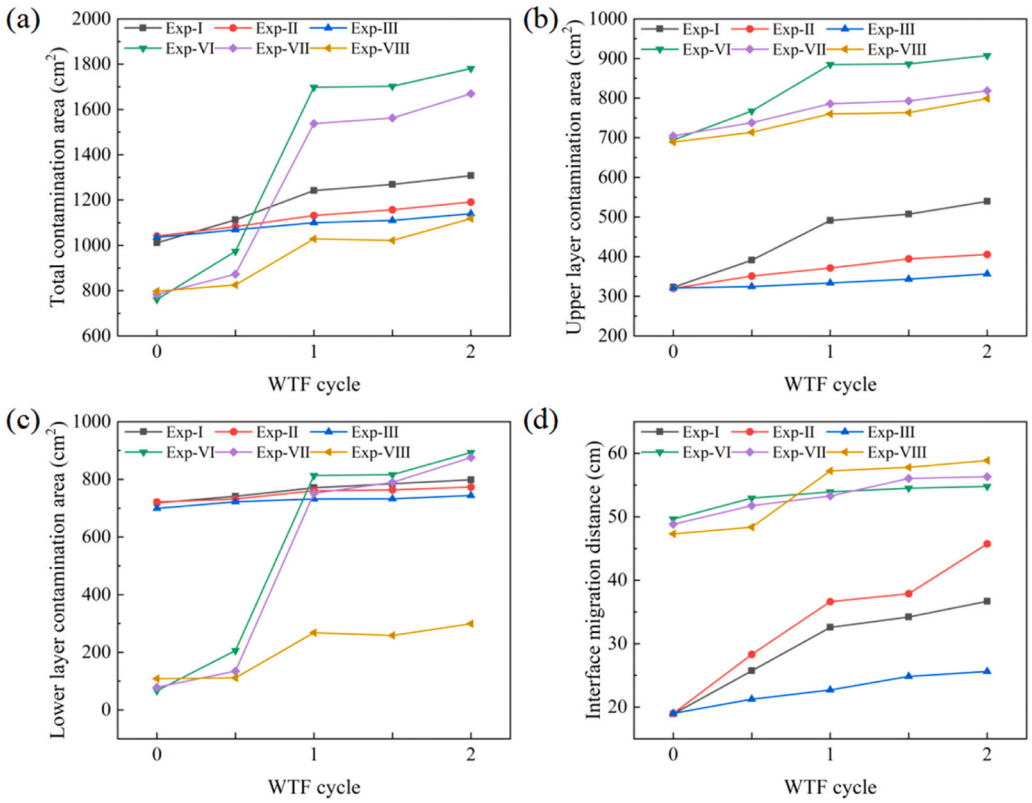

Fig. 6. Quantitative effects of WTF amplitudes on (a) total, (b) upper-layer, and (c) lower-layer contamination areas, and (d) interfacial migration distance.

the breakthrough of the capillary barrier. This theoretically predicted downward breakthrough was visually confirmed in the sand tank (Exp-VI and Exp-VII, as shown in Fig. 5d_3 and **5**e_3), leading to a substantial expansion of the total contaminated area (e.g., up to a 118.6% growth in Exp-VI as shown in Fig. 6a). In contrast, the 10 cm amplitude was a sub-threshold event. Due to the aforementioned spatial decoupling during the rising phase, the transmission of the transient hydraulic perturbation was physically blocked. As predicted by the spatially decoupled regime (Fig. 4), the interfacial capillary barrier remained intact, leaving the trapped LNAPL body undisturbed even after the falling phase (Fig. 5f_3).

In both configurations, higher amplitudes (30 cm and 20 cm) allowed the capillary fringe to submerge the interface, effectively mobilizing the trapped LNAPL. While the height of the capillary fringe increased with the water table amplitude, the magnitude of the redistribution response was nonlinearly related to this driving force. Specifically, while the 30 cm amplitude provided the maximum driving pressure for vertical breakthrough in F-C media, the lateral migration distance at the C-F interface followed a distinct hierarchy: 20 cm $>$ 30 cm $>$ 10 cm (Fig. 6d). This suggests a competitive relationship between the vertical driving pressure and the duration available for pore-scale lateral capillary wicking. An excessive amplitude may promote rapid vertical displacement at the expense of lateral plume expansion. While amplitude serves as the primary pressure driver for barrier failure, the initial water saturation state of the media further modulates the interfacial resistance, a mechanism as explored in Section 4.2.

4.1.3. Dominance of the first cycle and risk implications

Across all experimental sets, the first WTF cycle exerted the most significant influence on redistribution, with the growth rates of the total contaminated area in the second cycle significantly dropping (e.g., from 118.6% to 13.6% in Exp-VI), demonstrating the diminishing effect of successive fluctuations. This suggests that the initial fluctuation establishes the primary migration pathways, after which the system reaches a new quasi-equilibrium. The F-C structure, characterized by its sensitivity to breakthrough and subsequent rapid expansion in the underlying high-permeability coarse sand, presents higher environmental sensitivity in dynamic groundwater environments compared to the C-F structure.

4.2. Modulating spatial coupling (η_{max}) and pressure thresholds via initial water tables

The initial water table serves as a pre-conditioning factor that directly alters the initial water saturation at the stratified interface, and consequently modulates the effective dynamic head (Δh_{dyn}) during fluctuations. The sensitivity of the system to the initial WT is governed by the spatial coupling between the initial capillary fringe and the stratified interface. Fig. 7 compares the LNAPL distribution in C-F and F-C layered structures during two WTF cycles under different initial WT conditions: 0 and 3 cm for both structures, and an additional 15 cm for the F-C structure. The corresponding contamination area and the lateral migration distance along the stratigraphic interface are shown in Fig. 8. The statistical reliability of these measurements across replicate trials is confirmed by the low variability detailed in Figure S2 of the SI.

In the C-F configuration, even a 3 cm initial WT was sufficient to significantly alter the migration pattern. Based on the SWCCs (Fig. 2a), the high suction capacity of the fine sand established a characteristic capillary rise of approximately 18.6 cm above the water table. The resulting capillary fringe extended to a total height of 21.6 cm (18.6 cm rise + 3 cm WT). This placed the initial capillary water front adjacent to the C-F interface at 25 cm during the natural migration stage (Fig. 7b_1). It acted as a dynamic hydraulic cushion, trapping the downward-migrating LNAPL where gravitational and capillary forces reached a new equilibrium, specifically at a depth of 8.8 cm below the interface.

This coupling forced an early transition from vertical infiltration to lateral spreading across the tank width, a phenomenon absent in the dry initial condition. Interestingly, while the total contaminated area

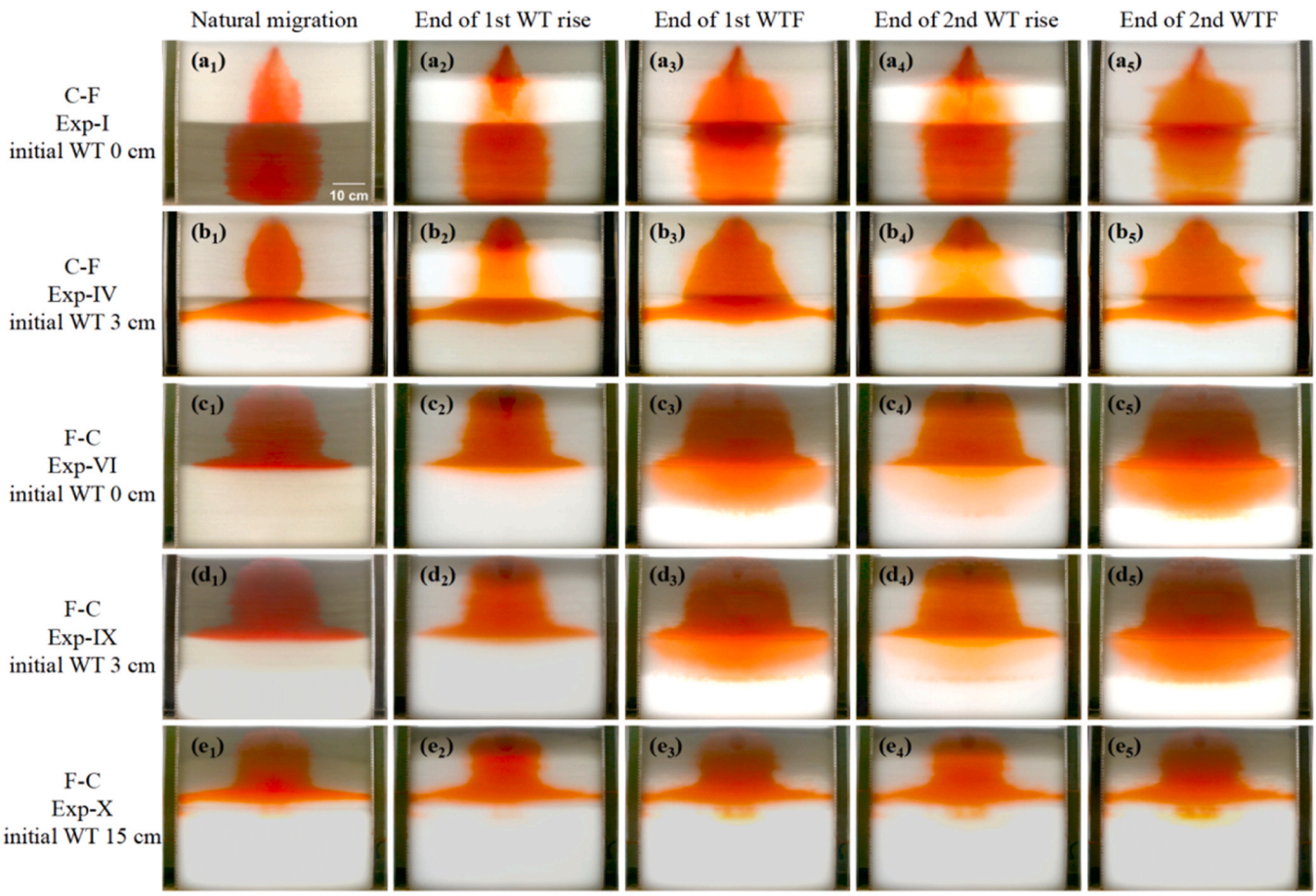

Fig. 7. Spatiotemporal distributions of LNAPL in C-F and F-C configurations, emphasizing the effects of different initial water table (WT) heights (0 cm, 3 cm, and 15 cm). Scale bar = 10 cm in the first sub-panels.

decreased due to inhibited vertical penetration (Fig. 8a), the upper-layer contamination area exhibited a more pronounced expansion risk. Specifically, the upper-layer growth rate reached 89.4% after two cycles in the 3 cm WT scenario, significantly exceeding the 67.1% observed in the dry scenario. This increased local risk but reduced global footprint suggests that the high initial water saturation at the interface enhances oil phase mobility and lateral wicking while trapping the bulk mass above the fine sand.

The response of the F-C structure follows a threshold-governed logic based on the characteristic capillary rise height of the underlying coarse sand, which was fitted at approximately 10.5 cm (Fig. 2a). During the natural migration stage, with a 3 cm initial WT, the capillary fringe reached a total height of only 13.5 cm (10.5 cm rise + 3 cm WT), remaining physically decoupled from the F-C interface at 25 cm. The intrinsic capillary barrier of the fine sand remained the primary regulator of entrapment. Consequently, the migration morphology remained largely consistent with the dry condition (Fig. 7c_1 vs. 7d_1). However, upon the introduction of the 30 cm amplitude WTF, the peak capillary fringe easily bridged the interface (yielding an identical maximum spatial coupling index $\eta_{max} = 1.62 \geq 1.0$). Combined with a highly sufficient driving pressure ($Bo^* = 3.10 > 1.0$), the system successfully transitioned into the dynamic breakthrough regime (Fig. 4), triggering massive downward mobilization during the falling phase.

With a 15 cm initial WT, however, the initial height of the capillary fringe (~10.5 cm rise + 15 cm WT > 25 cm) already effectively submerges the F-C interface (Fig. 7e_1). This initial interfacial submergence prepares the interface with high water saturation, facilitating a more uniform oil-water displacement front during the rising phase compared to the localized irregular diffusion observed in lower WT scenarios. During the falling phase, while breakthrough still occurred, the presence of the high initial WT altered the pressure balance. The WTF peaking at 30 cm generated an effective dynamic head (Δh_{dyn}) of 15 cm, yielding a $Bo^* \approx 1.72$. Because both the spatial prerequisite ($\eta_{max} = 1.62 \geq 1.0$) and the pressure threshold ($Bo^* > 1.0$) were satisfied, the system was firmly in the dynamic breakthrough regime (Fig. 4). However, the higher initial saturation in the underlying coarse sand increased displacement resistance. This led to a more constrained and laterally-distorted vertical plume, often forming an inverted trapezoidal shape due to the enhanced lateral driving effect of the residual water zone.

Across all configurations, a higher initial WT consistently resulted in a smaller total contaminated area after two WTF cycles (Fig. 8a). The presence of pre-existing water increases the resistance for LNAPL displacement, providing a protective buffer that limits deep vertical penetration. While capillary water coupling promotes lateral spreading at stratigraphic interfaces, it effectively reduces the overall volumetric footprint of the contamination. These results reveal that the environmental risk of LNAPL scales non-linearly with the initial groundwater depth. Specifically, the critically coupled state, where the initial capillary fringe meets the stratified interface, triggers the most complex redistribution patterns, and maximizes localized lateral spreading.

4.3. Validating kinetic allocation (Ca*) via fluctuation rates

While amplitude and initial WT dictate the threshold switches (η_{max} and Bo^*), the WTF rate introduces time-dependent constraints on LNAPL redistribution, validating the kinetic allocation mechanism governed by Ca^*. Fig. 9 compares the spatial distribution characteristics of LNAPL in the C-F and F-C structures under fluctuation rates of 40 mL/min and

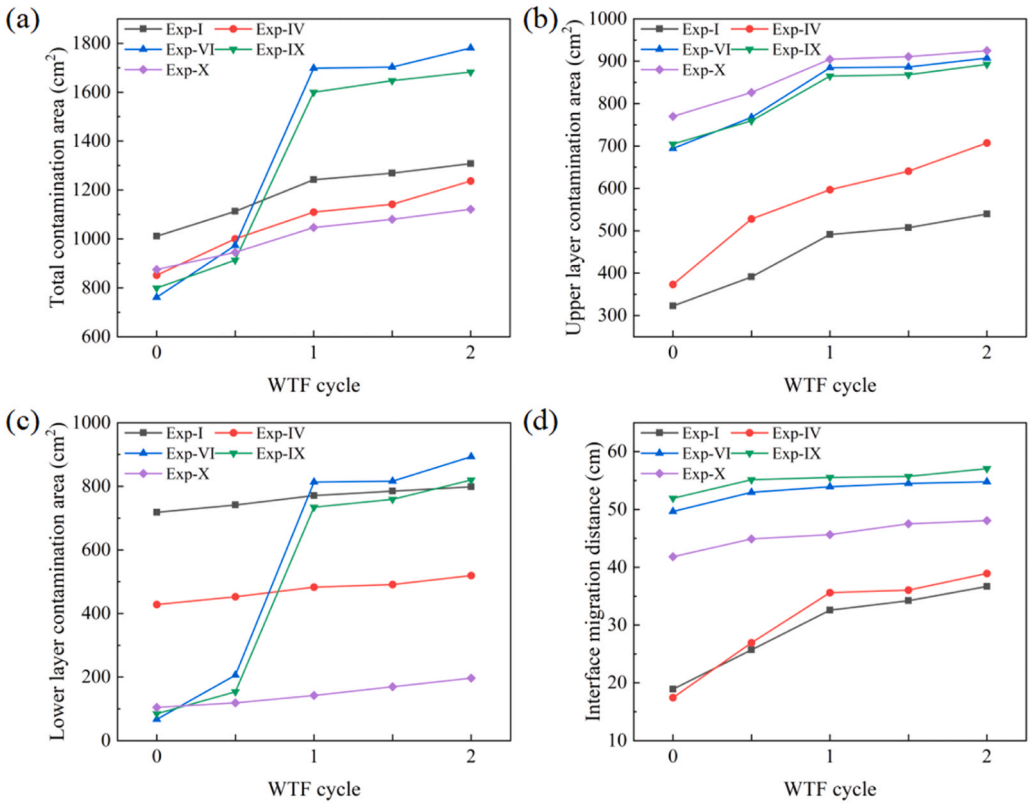

Fig. 8. Quantitative effects of initial water tables on (a) total, (b) upper-layer, and (c) lower-layer contamination areas, and (d) interfacial migration distance.

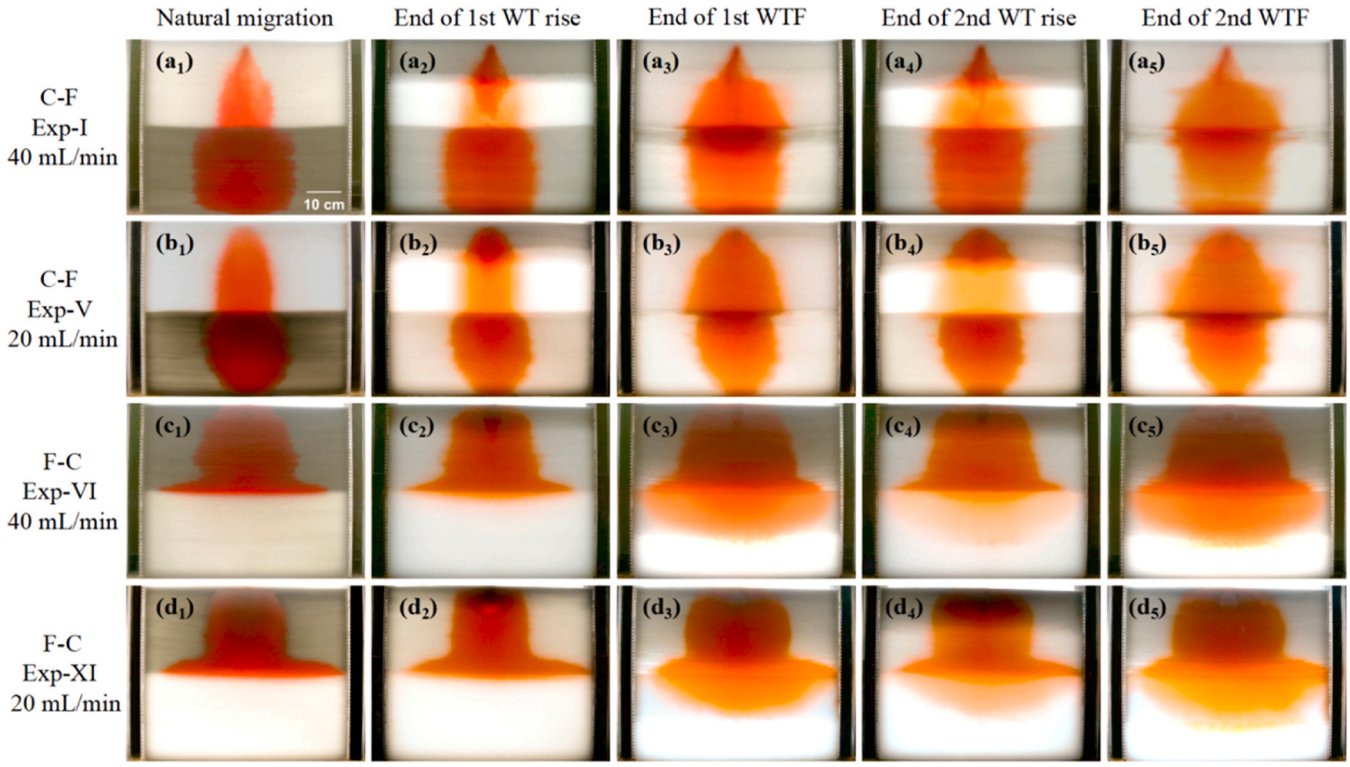

Fig. 9. Spatiotemporal distributions of LNAPL in C-F and F-C configurations, emphasizing the effects of different fluctuation rates (40 mL/min and 20 mL/min). Scale bar = 10 cm in the first sub-panels.

20 mL/min, with corresponding quantitative data in Fig. 10 (and associated error analyses in Figure S3 of the SI).

As theorized in Section 3.3, for stratified structures lacking a capillary barrier (i.e., the C-F structure), gravity naturally overcomes the

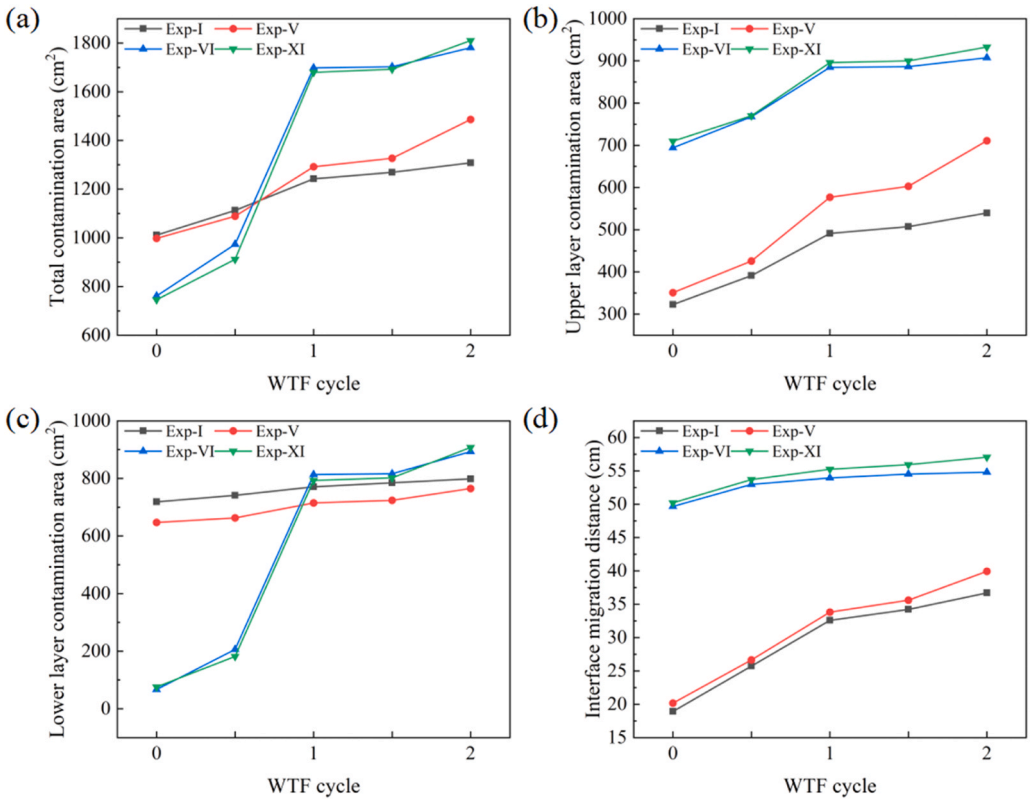

Fig. 10. Quantitative effects of fluctuation rates on (a) total, (b) upper-layer, and (c) lower-layer contamination areas, and (d) interfacial migration distance.

underlying displacement pressure. The primary WTF-induced risk is therefore controlled by kinetic allocation rather than vertical breakthrough. In the C-F configuration, LNAPL redistribution exhibited significant sensitivity to the fluctuation rate. A lower fluctuation rate (20 mL/min) proportionally reduces the macroscopic viscous displacement forces, corresponding to a lower Ca^*. To quantitatively link these parameters to the theoretical framework, the effective pore velocity (v_{pore}) was derived by dividing the volumetric fluctuation rates (40 and 20 mL/min) by the effective horizontal cross-sectional capacity of the tank system (which accounts for both the porous media volume and the open water table control zones). This translation yields specific Ca^* values of approximately 9.8×10^{-6} and 4.9×10^{-6}, respectively. This provides the multiphase system with an extended characteristic relaxation time during both rising and falling phases. This extended duration allows pore-scale lateral capillary wicking forces to dominate over vertical viscous displacement, facilitating a more pronounced lateral expansion in terms of contamination volume within the upper coarse sand layer (Fig. 9b_3 vs. 9a_3). During the second WTF cycle, the lower-rate scenario maintained a significantly higher growth rate in the upper-layer contamination area (23.2%) compared to the high-rate condition (9.8%) (Fig. 10b).

To quantitatively validate this, Fig. 11 illustrates the kinetic allocation phase by plotting the upper-layer contamination area against Ca^*. The steep rate dependency is visually evident: the lower Ca^* effectively translates to a significant expansion of the upper-layer contamination area (reaching approximately 711 cm^2), contrasting sharply with the viscous-dominated higher Ca^* baseline (approximately 530 cm^2 in Exp-I).

Conversely, the redistribution behavior in the F-C configuration remained largely insensitive to the fluctuation rate. The breakthrough of LNAPL in the F-C media is a threshold-controlled process governed primarily by whether the amplitude-driven pressure potential (Bo^*) reaches the entry pressure of the underlying coarse sand. Once the critical amplitude triggers barrier failure, the downward breakthrough

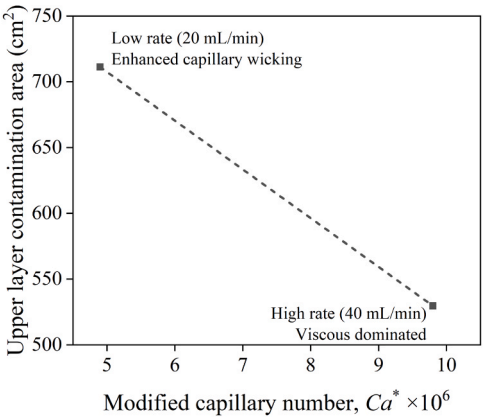

Fig. 11. For systems unconstrained by the capillary barrier (e.g., the C-F structure), the modified capillary number (Ca^*) serves as the kinetic regulator, dictating the extent of lateral capillary wicking quantified by the upper-layer contamination area.

occurs rapidly regardless of the kinetic rate. Consequently, the distribution morphology in the lower coarse sand, characterized by a semi-elliptical plume, showed no significant difference between the two scenarios (Fig. 9c_3 and 9d_3). Despite the overall insensitivity of the macroscopic plume shape, a lower rate resulted in slightly greater interfacial migration distances (Fig. 10d), confirming the universal but secondary role of contact time in interface-dominated transport.

The results indicate that the regulatory role of the fluctuation rate is fundamentally determined by the layered structure. For stratified structures lacking an interfacial capillary barrier (e.g., the C-F structure), slow-moving water tables significantly promote lateral plume expansion via pore-scale capillary wicking. Conversely, for barrier-limited systems (F-C), the dynamic risk is dictated by the dual

thresholds of spatial coupling (η_{max}) and driving pressure (Bo^*) rather than kinetic rates. This highlights the importance of considering fluctuation velocity and kinetic scaling parameters (Ca^*) in site-specific risk assessments, particularly for aquifers with high horizontal permeability.

4.4. Framework applicability and uncertainty analysis

4.4.1. Regime map validation and transferability

To synthesize the threshold-governed mechanisms of spatial coupling and macroscopic pressure balance, we propose a dimensionless regime map (Fig. 12). To validate this scaling framework beyond the specific geometry of our experimental setup, we mapped both our experimental data and well-documented benchmark datasets from the literature onto this phase space.

The regime map is governed by the critical theoretical boundaries of $\eta_{max} = 1.0$ and $Bo^* = 1.0$. When $\eta_{max} < 1.0$, the system remains in the spatially decoupled regime regardless of the potential dynamic head. Systems falling into this domain are hydrostatically stable because the perturbation is physically blocked. For instance, Exp-VIII remains trapped because the dynamic head is spatially decoupled from the interface ($\eta_{max} \approx 0.82 < 1.0$). When spatial coupling is achieved ($\eta_{max} \geq 1.0$) but the driving pressure is insufficient ($Bo^* < 1.0$), the system falls into the capillary sequestration regime. To externally validate this dual boundary of $\eta_{max} \geq 1.0$ and $Bo^* < 1.0$, we incorporated the 2D LNAPL infiltration experiment by Kechavarzi et al. [29]. Under a constant injection head of ≈ 18.3 cm against a capillary barrier with a displacement head of ≈ 55 cm, the calculated $Bo^* \approx 0.33$ is consistent with their observation of capillary trapping and lateral spreading above the fringe.

Only when both conditions are satisfied, i.e., $\eta_{max} \geq 1.0$ and $Bo^* > 1.0$, does the system enter the dynamic breakthrough regime. When the transient pressure overcomes the interfacial resistance, barrier failure occurs (e.g., Exp-VI, VII, IX, X, and XI). To demonstrate the applicability of this boundary across different driving mechanisms and fluid densities, we evaluated the classic DNAPL pooling experiments by Illangasekare et al. [30]. Note that applying this framework to DNAPL pools bridges two distinct physical forcing. While our LNAPL experiments are governed by the dynamic hydraulic forcing induced by transient water table fluctuations, where the LNAPL gravitational component is negligible, DNAPL pooling is driven by static buoyancy. Nevertheless, because Bo^* scales the total macroscopic driving pressure against pore-scale capillary resistance, both mechanisms can be evaluated using the same scaling approach. In gravity-driven DNAPL systems, this static buoyancy is translated into an equivalent dynamic head via a density correction: $\Delta h_{dyn} = H_{pool} \times \frac{\rho_{DNAPL} - \rho_w}{\rho_w}$. By extracting the critical pool height (H_{pool}) at the onset of downward fingering into the fine sand lens, the calculated Bo^* exceeds the 1.0 threshold.

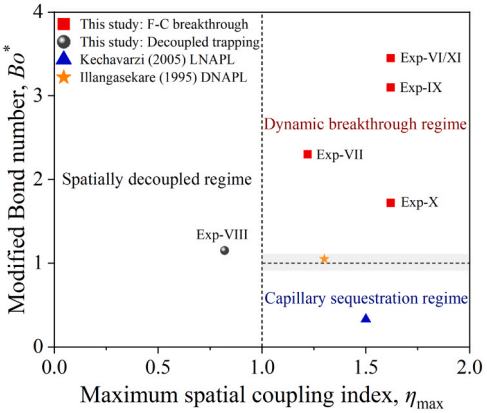

Fig. 12. Hydrodynamic regime map for NAPL redistribution in stratified porous media. External validations include LNAPL infiltration [29] and DNAPL pooling [30]. The shaded band indicates the probabilistic transition zone around $Bo^* = 1.0$ arising from parameter estimation uncertainty. For the external benchmark datasets, the contaminants were introduced directly above the capillary barrier, inherently satisfying $\eta_{max} \geq 1.0$. Thus, their specific horizontal positions are purely illustrative.

Notably, in both external datasets [29,30], the contaminant was introduced directly above the capillary barrier via injection or gravity pooling. Therefore, the spatial continuity prerequisite is inherently satisfied ($\eta_{max} \geq 1.0$). Their respective horizontal positions in Fig. 12 ($\eta_{max} = 1.50$ and 1.30) are purely illustrative to demonstrate the Bo^* pressure threshold. This validation demonstrates that the $Bo^* = 1.0$ boundary serves as a reliable hydrodynamic threshold for interfacial instability, regardless of whether the driving force originates from transient hydraulic gradients (LNAPLs) or static buoyancy (DNAPLs).

While we utilized classic well-documented macroscopic benchmark datasets (e.g., [29,30]) due to their rigorous provision of precise fluid-specific entry pressures and critical pool heights required for Bo^* calculation, this macroscopic threshold behavior aligns consistently with recent pore-scale and high-resolution numerical findings. For instance, recent studies by Yuan et al. [8] and Zuo et al. [4] have emphasized that transient multiphase redistribution is dictated by the instantaneous imbalance between local non-wetting phase pressure and capillary entry barriers. The proposed dual-threshold regime map links these microscopic kinetic principles to macroscopic boundary conditions, bridging the gap between classical multiphase flow physics and contemporary site-scale risk assessment needs.

From a mathematical modeling perspective, the proposed dimensionless framework serves as a macroscopic abstraction of classical multiphase flow equations. While highly non-linear mathematical models, such as the extended Darcy's law for multiphase flow and fractional flow formulations, can simulate detailed pore-scale dynamic displacement, they often require extensive site-specific parameterizations that are difficult to obtain in practice. By mathematically condensing the Young-Laplace equation into the macroscopic pressure threshold (Bo^*) and abstracting the fractional flow theory, which governs the rate-dependent allocation between viscous and capillary fluxes, into the kinetic regulator (Ca_{macro}), this framework translates complex theoretical models into a practical tool for environmental engineering applications.

4.4.2. Limitations and environmental implications

While the proposed dimensionless framework (η_{max}, Bo^*, Ca^*) outlines the macroscopic regimes of LNAPL redistribution, its extrapolation to site-scale scenarios requires recognizing inherent methodological constraints. First, the 2D quasi-planar geometry (2 cm width) of the sand tank inevitably introduces wall effects. The restricted transverse domain may artificially confine three-dimensional (3D) radial spreading, implying that the absolute lateral contamination area observed in the C-F structure serves as an amplified representation rather than a direct field equivalent. Additionally, reducing interfacial capillary barrier failure to a single macroscopic scalar threshold ($Bo^* = 1.0$) simplifies the complex pore-scale invasion percolation process, which can be influenced by localized micro-heterogeneities and fingering phenomena. Furthermore, the determinism of this threshold inherently relies on the analytical precision of the displacement pressure. Because the macroscopic displacement pressure (h_d) is derived via the maximum tangent method from the van Genuchten model, it is sensitive to the fitting uncertainty of the empirical retention curve parameters. Thus, the shaded probabilistic transition band depicted around $Bo^* = 1.0$ (Fig. 12) explicitly represents the error propagated from the 95% confidence intervals of α and n (Table S1). Physically, this statistical band acknowledges that macroscopic barrier failure is not an instantaneous binary event. In highly heterogeneous natural strata, localized micro-heterogeneities mean that invasion percolation occurs over a narrow pressure range. Finally, the system-level capillary number (Ca^*) assumes a bulk effective pore velocity (v_{pore}), which simplifies the

localized viscous fingering inherent to multiphase flow. Future micro-scale efforts must incorporate pore-scale velocity heterogeneity and dynamic contact angle hysteresis to refine these indices.

It is important to emphasize that the proposed phase diagram (Fig. 12) serves as a physically-grounded diagnostic framework rather than a deterministic universal map. When transitioning from this quasi−2D diagnostic framework to real 3D field-scale aquifers, the divergent scaling behaviors of the kinetic and threshold parameters must be carefully managed. In our experimental setup, the structural aspect ratio (L/d) remained geometrically constant, allowing the use of the simplified Ca^* as an effective kinetic regulator. However, to evaluate the actual extent of lateral spreading in complex 3D scenarios, the full macroscopic capillary number $Ca_{macro} = \frac{\mu v}{\sigma_{ow}} \times \frac{L}{d}$ must be reinstated. In real 3D scenarios, L represents the characteristic lateral macroscopic length scale of the contamination domain (or specific stratigraphic lens), and d is the representative pore-throat dimension. These extensive geometric parameters can be obtained through comprehensive site-specific characterizations, such as geophysical surveys to determine L, and advanced pore-scale analysis (e.g., mercury intrusion porosimetry on undisturbed core samples) to derive a statistically representative d field. Because L and d are highly stochastic in natural aquifers, the L/d ratio should be operationalized probabilistically. By coupling hydraulic tomography with stochastic geological modeling to generate a continuous L/d field, practitioners can translate the proposed deterministic boundaries into probabilistic risk maps, thereby accounting for subsurface heterogeneity.

In contrast, the modified Bond number $Bo^* = \frac{\Delta h_{dyn}}{h_{d(oil),coarse}}$ is defined through macroscopically measurable parameters, i.e., the dynamic water table fluctuation amplitude and the displacement pressure head of the coarse layer. The latter can be estimated from capillary retention curves of field cores or in-situ air-entry pressure measurements, avoiding the upscaling uncertainties inherent in extracting representative pore-throat dimensions from idealized geometric models or statistical pore-size distributions. In complex natural strata, effective capillary resistance is governed not by an idealized geometric pore radius, but by continuum-scale invasion percolation dynamics. Experimental derivation of h_d effectively captures the true macroscopic pressure threshold, accounting for bulk tortuosity and pore network connectivity, making Bo^* a robust and practical parameter for evaluating gravity-driven capillary barrier failure in heterogeneous field conditions. Together, these decoupled parameters ensure that the fundamental mechanisms of multiphase redistribution remain transferable to complex field-scale assessments.

Beyond these methodological considerations, the proposed dimensionless framework holds significant practical implications for the management of hazardous materials. Specifically, understanding the dynamic breakthrough regime (where $\eta_{max} \geq 1.0$ and $Bo^* > 1.0$) enables environmental engineers to identify critical water table fluctuation thresholds that could trigger the macroscopic failure of natural aquitards or engineered containment barriers. Furthermore, recognizing the kinetic allocation mechanism governed by Ca_{macro} provides a theoretical basis for predicting the lateral spread of toxic spills in highly permeable strata. To apply these theoretical boundaries in the field, practitioners could employ established high-resolution monitoring techniques. For instance, the dynamic hydraulic head (Δh_{dyn}) necessary for evaluating Bo^* can be continuously tracked using high-frequency pressure transducers in monitoring wells, while the spatial coupling index (η_{max}) can be verified non-invasively using time-lapse geophysical methods, such as electrical resistivity tomography, which is highly effective at capturing the dynamic boundaries of the capillary fringe relative to stratigraphic interfaces. By integrating these field-monitoring techniques with the theoretical boundaries established in this study, future site investigations can more reliably predict capillary barrier failures and the lateral expansion of hazardous plumes.

5. Conclusions

This study investigates the complex redistribution of LNAPL in stratified media under WTFs. The main findings are as follows:

(1) The redistribution of LNAPL is fundamentally governed by the stratified structure. The F-C structure acts as an interfacial capillary barrier that inhibits downward infiltration, while the C-F structure forces the downward flow to turn sideways, promoting lateral spreading along the interface.
(2) WTF amplitude serves as the primary pressure driver for the functional failure of the capillary barrier. In the F-C structure, amplitudes of 20 and 30 cm provide sufficient driving pressure to trigger vertical breakthrough. In contrast, the 10 cm amplitude is a sub-threshold event ($\eta_{max} < 1.0$). Its failure to bridge the spatial gap between the capillary fringe and the interface leaves the LNAPL body largely undisturbed.
(3) Initial water tables and fluctuation rates modulate the redistribution morphology. While higher initial water tables limit deep vertical penetration and reduce the total contaminated volumetric footprint, they significantly intensify localized lateral spreading above the C-F interface due to enhanced initial water saturation. Concurrently, lower fluctuation rates provide extended contact duration, allowing lateral capillary wicking to dominate over vertical viscous displacement, thereby maximizing the upper-layer contamination area.
(4) A generalized dimensionless framework based on a spatial coupling index (η_{max}), modified Bond number (Bo^*), and modified capillary number (Ca^*) is proposed. The critical phase boundaries of $\eta_{max} = 1.0$ and $Bo^* = 1.0$ partition the system into distinct stability regimes, while Ca^* acts as the kinetic regulator for unconstrained structures. This framework serves as a first-order macroscopic criterion for predicting interfacial capillary barrier stability, providing essential physical guidelines for dynamic risk assessment and management of hazardous materials. By shifting from empirical observations to this physics-based framework, environmental managers can prevent the critical underestimation of contamination footprints in highly dynamic subsurface environments, ultimately optimizing remediation designs and safeguarding vulnerable groundwater resources.

Environmental implication

Subsurface LNAPL contamination poses severe and long-term risks to dynamic groundwater systems. Traditionally, evaluating contaminant redistribution under transient water tables relies on specific experimental observations, making field-scale extrapolation challenging. This study overcomes this limitation by establishing a generalized and dimensionless framework that decouples the multiscale physical processes governing multiphase flow. Utilizing a maximum spatial coupling index (η_{max}), a modified Bond number (Bo^*), and a modified capillary number (Ca^*), this framework provides first-order predictive boundaries for capillary barrier failure and toxic plume expansion. These insights offer physics-based guidelines for evaluating aquifer vulnerability and optimizing targeted remediation strategies.

CRediT authorship contribution statement

Zhimin Ao: Writing – review & editing, Project administration, Funding acquisition. **Didi Li:** Writing – review & editing, Writing – original draft, Project administration, Funding acquisition, Conceptualization. **Kun Luo:** Visualization, Investigation, Conceptualization.

Declaration of Competing Interest

The authors declare that they have no known competing financial

interests or personal relationships that could have appeared to influence the work reported in this paper.

Acknowledgements

This study was supported by the National Natural Science Foundation of China (Grant No. T2421005, and 41807191), and the Guangzhou Science and Technology Planning Project (Grant No. 2023A04J0918).

Appendix A. Supporting information

Supplementary data associated with this article can be found in the online version at doi:10.1016/j.jhazmat.2026.142776.

Data Availability

Data will be made available on request.

References

[1] Cavelan, A., Faure, P., Lorgeoux, C., Colombano, S., Deparis, J., Davarzani, D., Enjelvin, N., Oltean, C., Tinet, A.-J., Domptail, F., 2024. An experimental multi-method approach to better characterize the LNAPL fate in soil under fluctuating groundwater levels. J Contam Hydrol 262, 104319.
[2] Onaa, C., Olaobaju, E.A., Amro, M.M., 2021. Experimental and numerical assessment of Light Non-Aqueous Phase Liquid (LNAPL) subsurface migration behavior in the vicinity of groundwater table. Environ Technol Innov 23, 101573.
[3] Han, K., Zuo, R., Qin, R., Xu, D., Zhao, X., Pan, M., Liu, J., Xu, Y., Wang, J., 2025. Effect and mechanism of the moisture content on the kinetic retardation of LNAPL pollutant migration by the capillary zone. J Hazard Mater 487, 137266.
[4] Zuo, R., Wu, Z., Liu, J., Zheng, S., Xu, Z., Wang, Z., Xue, Z., Wang, C., 2025. Construction and application of a quantitative model for calculating LNAPL lateral migration in the capillary zone. J Hazard Mater, 139321.
[5] Kechavarzi, C., Soga, K., Illangasekare, T., Nikolopoulos, P., 2008. Laboratory study of immiscible contaminant flow in unsaturated layered sands. Vadose Zone J 7, 1–9.
[6] Simantiraki, F., Aivalioti, M., Gidarakos, E., 2009. Implementation of an image analysis technique to determine LNAPL infiltration and distribution in unsaturated porous media. Desalination 248, 705–715.
[7] Li, D., Cai, D., Ao, Z., Jiang, X., 2023. Migration and redistribution of LNAPL in inclined stratified soil media. J Hazard Mater 447, 130809.
[8] Yuan, C., Yin, Y., Hu, X., Yu, X., Li, Y., 2025. Experimental and numerical simulation study on quantitative assessment of LNAPL migration behavior in porous media. J Hydrol 651, 132619.
[9] Wei, Y., Chen, Y., Cao, X., Xiang, M., Huang, Y., Li, H., 2024. A critical review of groundwater table fluctuation: Formation, effects on multifields, and contaminant behaviors in a soil and aquifer system. Environ Sci Technol 58, 2185–2203.
[10] Alazaiza, M.Y., Ramli, M.H., Copty, N.K., Sheng, T.J., Aburas, M.M., 2020. LNAPL saturation distribution under the influence of water table fluctuations using simplified image analysis method. Bull Eng Geol Environ 79, 1543–1554.
[11] Koohbor, B., Colombano, S., Harrouet, T., Deparis, J., Lion, F., Davarzani, D., Ataie-Ashtiani, B., 2023. The effects of water table fluctuation on LNAPL deposit in highly permeable porous media: A coupled numerical and experimental study. J Contam Hydrol 256, 104183.
[12] Almaliki, D.F., Ramli, H., Zaiter, A., 2025. Experimental investigation of single and intermittent light non-aqueous phase liquid spills under dynamic groundwater. Civ Eng J 11, 290–307.
[13] Tareq al-Hussain, O., Ramli, H., Al-Haidarey, M.J., Naser, H.Y., 2025. Detecting LNAPL migration in real time using electrical resistivity and statistical models. Sci Rep 15, 17430.
[14] He, Z., Liang, F., Meng, J., Li, N., 2022. Effects of groundwater fluctuation on migration characteristics and representative elementary volume of entrapped LNAPL. J Hydrol 610, 127833.
[15] Alazaiza, M.Y., Ngien, S.K., Copty, N., Bob, M.M., Kamaruddin, S.A., 2019. Assessing the influence of infiltration on the migration of light non-aqueous phase liquid in double-porosity soil media using a light transmission visualization method. Hydrogeol J 27, 581–593.
[16] Zuo, R., Zhao, X., Yang, J., Pan, M., Xue, Z., Gao, X., Wang, J., Teng, Y., 2021. Analysis of the LNAPL migration process in the vadose zone under two different media conditions. Int J Environ Res Public Health 18, 11073.
[17] Pan, Y., Zhang, Q., Yu, Y., Tong, Y., Wu, W., Zhou, Y., Hou, W., Yang, J., 2021. Three-dimensional migration and resistivity characteristics of crude oil in heterogeneous soil layers. Environ Pollut 268, 115309.
[18] Zheng, J., Yang, Y., Li, J., Zhang, H., Ma, Y., 2023. The migration mechanism of BTEX in single-and double-lithology soil columns under groundwater table fluctuation. Toxics 11, 630.
[19] Zhou, J., Pan, M., Chang, C., Wang, A., Wang, Y., Lyu, H., 2022. Migration law of LNAPLs in the groundwater level fluctuation zone affected by freezing and thawing. Water 14, 1289.
[20] Engelmann, C., Schmidt, L., Werth, C.J., Walther, M., 2019. Quantification of uncertainties from image processing and analysis in laboratory-scale DNAPL release studies evaluated by reflective optical imaging. Water 11, 2274.
[21] Shen, H., Huang, Y., Su, Y., Miao, K., Jiang, Y., 2023. Experimental investigation of light non-aqueous phase liquid mobilization in filled fractured network media. Environ Sci Pollut Res 30, 32628–32640.
[22] Zhao, G., Cheng, J., Jia, M., Zhang, H., Li, H., Zhang, H., 2024. The effect characterization of lens on LNAPL migration based on high-density resistivity imaging technique. Appl Sci -Basel 14, 10389.
[23] Sharma, R.S., Mohamed, M.H., 2003. An experimental investigation of LNAPL migration in an unsaturated/saturated sand. Eng Geol 70, 305–313.
[24] Yao, M., Yuan, Q., Qu, D., Liu, W., Zhao, Y., Wang, M., 2022. Effects of airflow rate distribution and nitrobenzene removal in an aquifer with a low-permeability lens during surfactant-enhanced air sparging. J Hazard Mater 437, 129383.
[25] Van Genuchten, M.T., 1980. A closed-form equation for predicting the hydraulic conductivity of unsaturated soils. Soil Sci Soc Am J 44, 892–898.
[26] Hilfer, R., Øren, P.E., 1996. Dimensional analysis of pore scale and field scale immiscible displacement. Transp Porous Media 22, 53–72.
[27] Armstrong, R.T., Georgiadis, A., Ott, H., Klemin, D., Berg, S., 2014. Critical capillary number: Desaturation studied with fast X-ray computed microtomography. Geophys Res Lett 41, 55–60.
[28] Pennell, K.D., Pope, G.A., Abriola, L.M., 1996. Influence of viscous and buoyancy forces on the mobilization of residual tetrachloroethylene during surfactant flushing. Environ Sci Technol 30, 1328–1335.
[29] Kechavarzi, C., Soga, K., Illangasekare, T.H., 2005. Two-dimensional laboratory simulation of LNAPL infiltration and redistribution in the vadose zone. J Contam Hydrol 76, 211–233.
[30] Illangasekare, T.H., James, J., Ramsey, L., Jensen, K.H., Butts, M.B., 1995. Experimental study of movement and distribution of dense organic contaminants in heterogeneous aquifers. J Contam Hydrol 20, 1–25.